NANO LETTERS

Letter

pubs.acs.org/NanoLett

Using X-ray Microscopy To Understand How Nanoporous Materials Can Be Used To Reduce the Large Volume Change in Alloy Anodes

John B. Cook,[†] Terri C. Lin,[†] Eric Detsi,[†,⊥] Johanna Nelson Weker,[‡] and Sarah H. Tolbert*[,†,§,∥]

[†]Department of Chemistry and Biochemistry, UCLA, Los Angeles, California 90095, United States

[‡]Stanford Synchrotron Radiation Lightsource, SLAC National Accelerator Laboratory, Menlo Park, California 94025, United States

[§]Department of Materials Science and Engineering, UCLA, Los Angeles, California 90095, United States

[∥]The California NanoSystems Institute, UCLA, Los Angeles, California 90095, United States

Supporting Information

ABSTRACT: Tin metal is an attractive negative electrode material to replace graphite in Li-ion batteries due to its high energy density. However, tin undergoes a large volume change upon alloying with Li, which pulverizes the particles, and ultimately leads to short cycling lifetimes. Nevertheless, nanoporous materials have been shown to extend battery life well past what is observed in nonporous material. Despite the exciting potential of porous alloying anodes to significantly increase the energy density in Li-ion batteries, the fundamental physics of how nanoscale architectures accommodate the electrochemically induced volume changes are poorly understood. Here, operando transmission X-ray microscopy has been used to develop an understanding of the mechanisms that govern the enhanced cycling stability in nanoporous tin. We found that in comparison to dense tin, nanoporous tin undergoes a 6-fold smaller areal expansion after lithiation, as a result of the internal porosity and unique nanoscale architecture. The expansion is also more gradual in nanoporous tin compared to the dense material. The nanoscale resolution of the microscope used in this study is ∼30 nm, which allowed us to directly observe the pore structure during lithiation and delithiation. We found that nanoporous tin remains porous during the first insertion and desinsertion cycle. This observation is key, as fully closed pores could lead to mechanical instability, electrolyte inaccessibility, and short lifetimes. While tin was chosen for this study because of its high X-ray contrast, the results of this work should be general to other alloy-type systems, such as Si, that also suffer from volume change based cycling degradation.

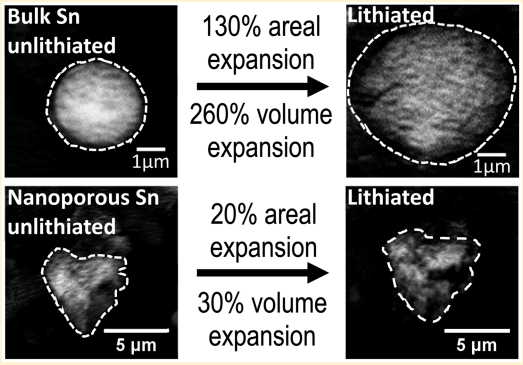

KEYWORDS: *Li-ion battery, alloy anodes, tin, transmission X-ray microscope, operando, in situ, porous tin, porous silicon*

Graphite has been used as the anode in most Li-ion batteries for over 20 years because of its ability to reversibly intercalate Li-ions, its high electronic conductivity, its low volume change during cycling, and its long cycle lifetime.[1−4] Even though graphite is a widely used negative electrode in commercial applications, its low capacity for Li-ions (one Li-ion per six carbon atoms) and low density lead to a mediocre gravimetric storage capacity of 372 mAh/g and volumetric storage capacity of 756 mAh/cm^3.[5−7] In response to a desire for higher energy density Li-ion batteries, research on materials that electrochemically alloy with lithium ions has become extremely active because these materials can store significantly more energy through multielectron processes.[5,8−12] Tin is an attractive candidate for high energy density applications because of its high gravimetric storage capacity of 960 mAh/g and volumetric storage capacity of 1990 mAh/cm^3 combined with high electrical conductivity.[5,13,14] One significant issue that has limited the use of tin in commercial applications (along with most other alloy-type materials) is that tin expands ∼300% upon alloying with Li, resulting in the rapid decay of capacity with cycling.[11,13,15−19] These volume changes lead to deformations like cracking, and repeated irreversible electrolyte decomposition on these freshly formed cracked surfaces.[16,17,20,21] These degradation processes ultimately lead to electrical isolation of large portions of the active material, which then no longer contribute to the capacity of the battery.

Nanostructuring tin and other alloy-type materials is a proven technique to mitigate the above-mentioned cycling induced degradation. A common failure mechanism in alloy-type materials arises from inhomogeneous volume changes within a particle due to limited Li-ion diffusion kinetics.[9] The lithiation of tin first begins at the outermost surfaces in contact with the electrolyte. Because of limited solid-state lithium-ion diffusion rates in tin, the outer surface expands more rapidly than the inner core. This volume mismatch of the lithium rich and lithium deficient phases then lead to interfacial strain build-

Received: October 6, 2016
Revised: December 23, 2016
Published: January 5, 2017

DOI: 10.1021/acs.nanolett.6b04181
Nano Lett. 2017, 17, 870−877

up. Typically, the strain is relieved by crack propagation, which degrades the active material. Reducing the dimension of the particles decreases the diffusion pathlengths and promotes homogeneous lithiation/delithiation within a single particle. In practice, small tin nanocrystals have been shown to improve cycle lifetimes compared to their bulk counterparts.[22−24] However, the main disadvantage of using small nanocrystals is the large interparticle contact resistance as a result of these material's intrinsically high surface area.

Nanoporous structures are ideal architectures to resolve the aforementioned issues. The Tolbert group has recently developed methods to create nanoporous tin by selective dealloying of a comelted Sn/Mg alloy that can be cycled 350 times while retaining over 72% of the initial capacity.[25,26] This material will be used in the studies presented here because it is an excellent material platform to understand how porosity can enable long cycle lifetimes in high capacity alloy-type anode materials. Additionally, various porous silicon[27−33] and porous tin oxide[34−36] architectures have also been shown to significantly increase the cycle lifetimes of these high capacity alloy-type materials compared to the dense nonporous form. While these studies offer practical solutions for increasing the lifetimes of alloy-type materials, it is not well understood how the volume change is actually accommodated in these porous structures.

Various techniques have been used to understand the structural and chemical changes of electrode materials during cycling.[19,37−49] In particular, microscopy techniques such as transmission electron microscopy (TEM) and transmission X-ray microscopy (TXM), especially when performed during the operation of an electrochemical system (operando), are powerful tools to understand the connection between nanoscale architecture and cycling performance. For example, TEM has been used to follow the alloying reaction of a single SnO_2 nanowire, which provided a visual understanding of the lithiation mechanism and the huge anisotropic volume change in those one-dimensional (1D) materials.[19] While TEM has several advantages, it is generally limited to imaging thin specimens in a small field of view. These constraints preclude the study of thick samples in their native electrode environment so that the TEM results never represent actual operating conditions. TXM addresses these limitations, and the large field of view, high flux, and hard X-ray radiation make this technique well suited for studying battery materials in their native slurry electrode environment with nanoscale resolution.[38−40] Indeed, TXM has been used for a variety of operando studies, including studies of bulk tin, Li-sulfur, and bulk germanium.[38−44] In all cases, the direct imaging of these active materials during the operation of the battery has led to a fundamental understanding of the mechanisms responsible for structural changes that occur during charge storage.

In this study, we utilize synchrotron-based TXM to study the effects of porosity on the volume change occurring in tin during the electrochemical alloying and dealloying reaction with lithium. We compare micrometer size dense tin to nanoporous tin created by selective dealloying. Our results indicate that the porous nanostructured tin expands significantly less than bulk tin due to the internal void space of the pores. We find that TXM is an excellent method to examine both the nanoscopic changes of the porous material along with the micrometer level changes that are occurring in individual tin particles.

We recently reported a novel method for preparing porous tin with a hierarchical granular morphology by selectively dealloying magnesium from a $Sn_{15}Mg_{85}$ alloy.[25] The synthesis method produces 1−10 μm diameter grains that are comprised of an interconnected 3D nanoporous structure with ∼25% internal porosity. This nanoporous tin (NP-Sn) material showed excellent capacity retention with 72% retention after 350 cycles when cycled in a traditional slurry electrode vs lithium metal. The high reversibility of this material makes this system an ideal platform to study how nanoscale porosity influences electrochemical stability in alloy-type materials.

For this work, we synthesized NP-Sn according to the methods already established in our previous report.[25] The XRD pattern of this dealloyed NP-Sn powder is shown in Figure S1, and is consistent with tetragonal tin (JCPDS no. 00-004-0673). The SEM images shown in Figure 1a,b clearly show the intrinsic porous nanoscale architecture of the tin particles. The backscattered SEM image in Figure 1c shows an NP-Sn particle (bright) in a carbon fiber-based electrode; here the dark striations are carbon fibers. This SEM image demonstrates that the ball milling process used to incorporate the hydrophobic carbon fibers and the NP-Sn into the aqueous binder does not modify the morphology of the NP-Sn. Finally, the TXM image presented in Figure 1d, shows the edge of a pristine NP-Sn particle before cycling. The image shows similar spherical pores to those observed in the backscattered SEM image in Figure 1c. The TXM image demonstrates the excellent contrast and resolution afforded by this X-ray microscope.

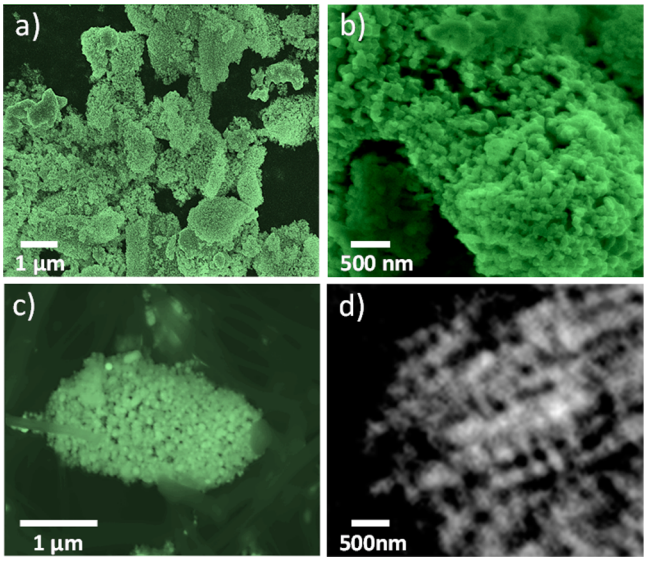

Figure 1. Microscopy characterization of NP-Sn. Secondary electron images of NP-Sn showing particles between 1 and 10 μm that are comprised of an interconnected network of tin nanoligaments and nanopores (a,b). Higher resolution images suggest hierarchical porosity extending down to the nanometer length scale. Backscattered image of NP-Sn after ball mill slurry processing showing that these structures are not compromised during the vigorous mixing process (c). Transmission X-ray microscopy image of NP-Sn demonstrating the nanoscale resolution of this technique that allows visualization of many of the nanoscale pores and ligaments (d).

NP-Sn was further analyzed using nitrogen porosimetry (Figure 2). The nitrogen isotherm of NP-Sn shown in Figure 2a displays hysteresis above 0.5 P/P_0 indicating the presence of mesoporosity.[50,51] The Barrett−Joyner−Halenda (BJH)[50] cumulative pore volume versus pore width plot in Figure 2b shows that ∼60% of the pore volume derives from pores that

DOI: 10.1021/acs.nanolett.6b04181
Nano Lett. 2017, 17, 870−877

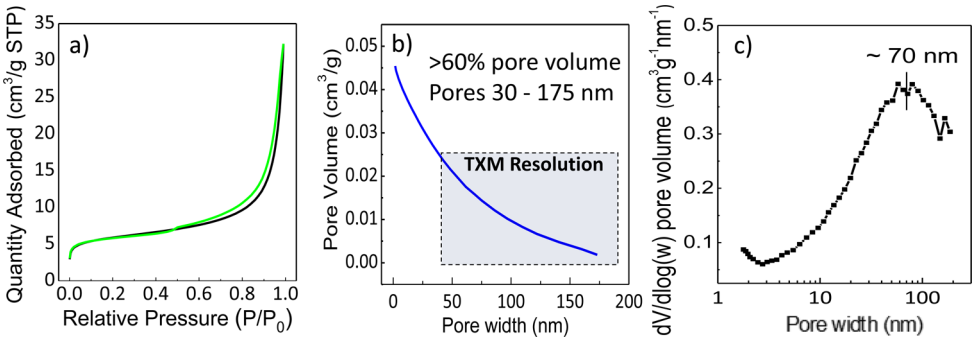

Figure 2. Nitrogen adsorption analysis on NP-Sn. Nitrogen isotherm at 77K of NP-Sn displaying hysteretic behavior above 0.5 P/P_0 indicating the presence of meso and macropores (a). Cumulative pore volume versus pore width trace, which was derived from the adsorption branch of the nitrogen isotherm (b). The total pore volume is 0.045 cm^3/g, which is used to calculate the porosity of NP-Sn as ~25%. In addition, this plot shows that more than 60% of the pore volume is within the resolution limit of the transmission X-ray microscope used to study this material. Barrett−Joyner−Halenda pore-size distribution calculated from the adsorption branch of the nitrogen isotherm (c). The average pore size is ~70 nm, and this value is indicated in the plot.

are within the resolution limit of the microscope on beamline 6-2 at the Stanford Synchrotron Radiation Lightsource (>30 nm). The total pore volume between 20−200 nm is 0.045 cm^3/g. Using that pore volume, the percent porosity of NP-Sn is calculated to be 25%. The average pore size of NP-Sn was also calculated from the adsorption branch of the nitrogen isotherm using the BJH model (Figure 2c). The peak value on the plot corresponds to the average pore width, which is calculated to be ~70 nm. As we mentioned previously, it is generally accepted that porous structures with smaller pores, such as the one described here, are better able to accommodate volume expansion and increase cycle lifetimes.[25,27−30,32,34−36,52] Through operando TXM, we directly observe the mechanisms responsible for the increased cycle lifetime. We expect the results can be applied to various other alloy-type materials like silicon and germanium.

The electrochemical lithiation and delithiation of tin proceeds through a number of distinct crystalline Li-Sn phases.[53,54] The first crystalline lithiation product of Sn is a Li_2Sn_5 phase, which forms at about 0.760 V versus Li/Li^+ at 25 °C.[54] The maximum theoretical capacity of tin is 990 mAh/g, corresponding to the $Li_{22}Sn_5$ phase, which begins to forms around 0.380 V versus Li/Li^+ at 25 °C.[14,54,55] Volume expansion occurs during lithiation as a result of the added Li volume and the formation of lower density Li−Sn phases. As mentioned above, the porous tin we developed cycles reversibly as a result of its unique nanoscale architecture, despite the large intrinsic volume changes that occur during alloying of Sn with Li. The cycling lifetime characteristics of micrometer spherical tin powder, and NP-Sn powder in a slurry electrode is shown in Figure 3a, which demonstrates the lifetime enhancement porosity affords this material system. The nonporous tin performs as expected, and quickly fails after ~5 cycles, while NP-Sn delivers its capacity stably over a much longer interval. By comparing the structural evolution of both dense tin and the robust NP-Sn, we aim to develop a structural understanding of just how porous structures accommodate volume expansion during cycling.

For these experiments, X-ray transparent electrochemical pouch cells[8] were galvanostatically cycled to drive the Li insertion and deinsertion process. SEM images of the working electrodes (thickness <10 μm) are shown in Figure S2. The galvanostatic traces of dense tin and NP-Sn collected during the operando measurement are shown in Figure 3b,c, respectively.

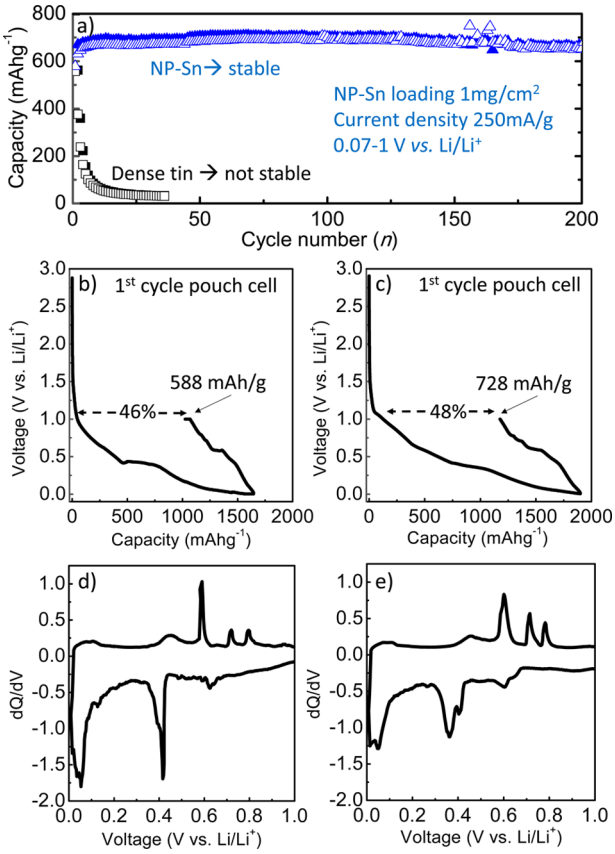

Figure 3. Capacity versus cycle number obtained from NP-Sn and dense tin slurry electrodes made with a 65:20:15 ratio of active material/carbon fiber/CMC with a 1 mg/cm^2 mass loading, cycled at a current density of 250 mA/g (a). Voltage versus capacity plots of dense tin (b) and NP-Sn (c) normalized by only the mass of tin in the electrode collected during the TXM experiment. The current density used for the dense tin electrodes was 356 mA/g, and the current density used for NP-Sn was 724 mA/g. Plots of dQ/dV for dense tin (d) and NP-Sn (e) showing typical profiles for the lithiation/delithiation of tin. The dQ/dV profile for NP-Sn is broadened compared to dense tin, indicative of the nanoscopic nature of the material.

As a result of the nanoporous architecture, the deinsertion process of NP-Sn delivers a capacity of 728 mAh/g compared to 588 mAh/g for dense tin, demonstrating better utilization of

DOI: 10.1021/acs.nanolett.6b04181
Nano Lett. 2017, 17, 870−877

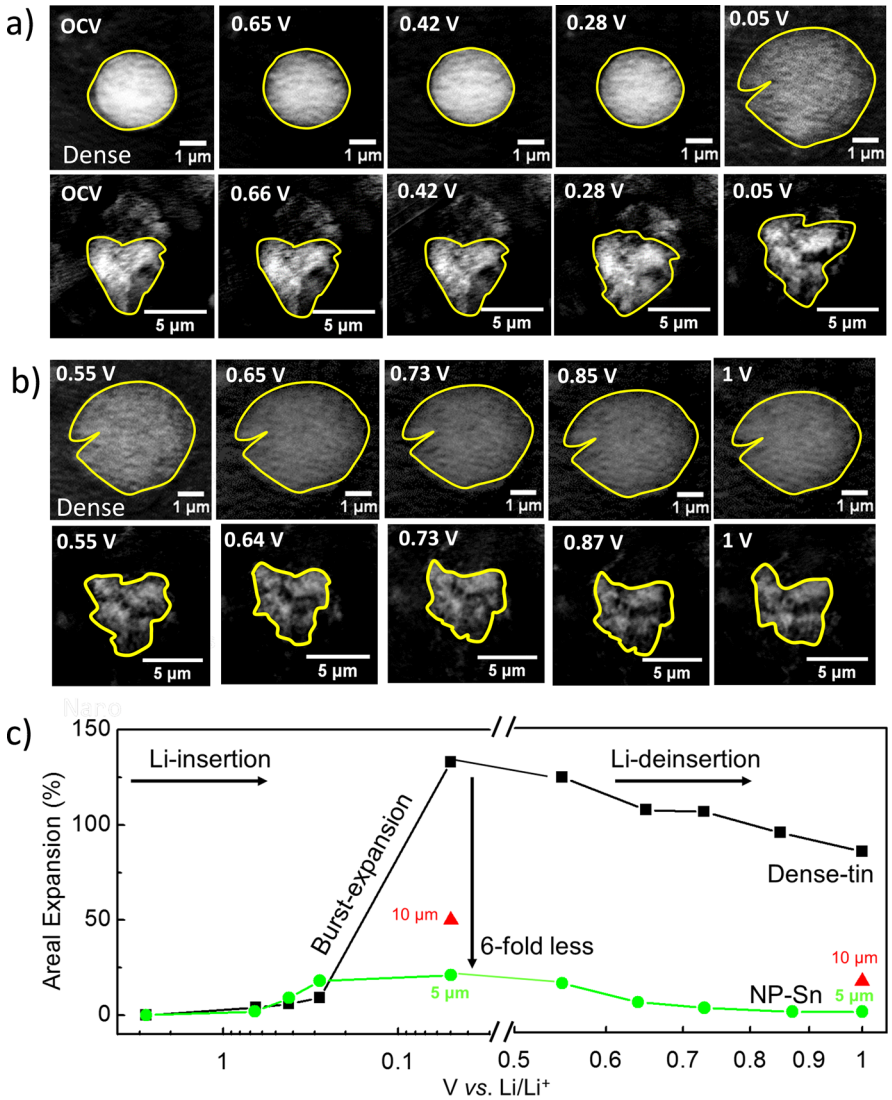

Figure 4. Absorption images of dense and nanoporous tin collected in an X-ray transparent pouch cell using a transmission X-ray microscope operating at 8.95 keV. Part (a) shows data collected with decreasing voltage (left-to-right), corresponding to increasing Li-concentrations. Dense tin (top) undergoes a burst-expansion mechanism, which occurs predominantly at the end of the insertion process. This process leads to tremendous strain in the material followed by crack formation observed at 0.05 V. The NP-Sn (bottom) expands less than dense tin and evolves to the final lithiated state more homogeneously. Part (b) shows data collected with increasing voltage (left-to-right), corresponding to decreasing Li-concentrations. Dense tin (top) was found to be irreversibly deformed and does not return to its original shape or size. Cracks formed during lithiation remain in the material. By contrast, the nanostructured NP-Sn (bottom) contracts back nearly to its original size, leading to the long cycle lifetimes of this material. Part (c) shows quantification of the areal expansion of the TXM images in this figure. Percent areal expansion is shown for dense tin (black squares), 5 μm NP-Sn (green circles), and 10 μm NP-Sn (red triangles) at different voltages and thus different lithiation states.

the active material. The dQ/dV traces of dense tin (Figure 3d) and NP-Sn (Figure 3e) show the typical voltage signatures for the lithiation/delithiation of tin. The dQ/dV profiles for NP-Sn are broader than dense tin due to the high surface area of the material, which has been reported previously.[24] We note that in order to image single NP-Sn particles with TXM, a large percentage of carbon fibers (~55%) was used in these electrodes to decrease the particle loading density, which isolates just a few particles within the microscope's 38 μm field of view (see Figure S2 for SEM images of these low density electrodes). However, this leads to a poor first cycle efficiency (~47%). The carbon fibers used in this study are a graphitic form of carbon with significant crystalline defect density, which tends to trap lithium ions leading to poor reversibility in the carbon fibers component of the electrode.[56] The irreversibility in the first insertion process is thus comprised of irreversibility from solid electrolyte interphase (SEI) formation, along with irreversibility from lithium ion trapping in the carbon fibers. We should note that these processes do not affect the TXM imaging because the X-ray absorption cross-section of these decomposition products are negligible compared to Sn at this X-ray energy and so neither the carbon fibers nor the SEI can be seen. In the following section, we display TXM images that correspond to the galvanostatic traces in Figure 3, and make correlations between structure and electrochemistry.

The images shown in Figure 4 were collected from samples in X-ray transparent pouch cells using TXM during continious galvanostatic cycling. Two different 38 μm × 38 μm regions were imaged (~10−20 s delay between regions) with a 6 min delay between images in the same region. Working directly below the Cu K-shell absorption edge (8.98 keV) afforded excellent X-ray transmission through the 9 μm thick copper

DOI: 10.1021/acs.nanolett.6b04181
Nano Lett. 2017, 17, 870−877

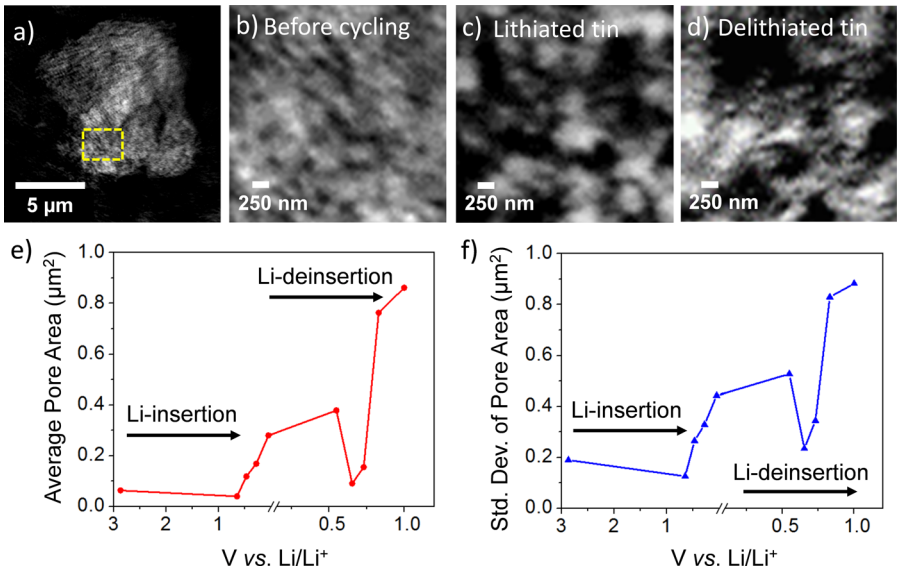

Figure 5. Absorption images and pore analysis for a larger NP-Sn particle collected using TXM; image contrast has been adjusted to increase visibility. (a) The full NP-Sn grain used for the pore evolution study. The yellow square indicates the area we focused on in order to track the same pores throughout cycling. (b-d) The magnified TXM images before cycling (b), in the lithiated state (c), and in the delithiated state (d). (e,f) The average pores size and standard deviation of the pores size at each voltage plateau throughout lithiation and delithiation. Both pore size and pores size distribution increase upon lithiation due to the volume expansion. Pore size and pore size distribution first decrease upon delithiation due to volume contraction. Both metrics then increase at full delithiation as some pores crack and due to the volume change, resulting in a bimodal pores size distribution with a few very large pores. Despite the pore size changes, the interconnections of the nanotin based ligaments appear to be uninterrupted; interconnected pores and ligaments are fundamental to the favorable performance of this system.

current collector and provided excellent contrast between tin and other battery components. The dense tin particle in Figure 4a (top) clearly shows expansion and crack propagation as the Li-concentration increases, which has been reported previously using TXM.[41,43,44] We have defined the percent areal expansion in eq 1

$$\%\mathrm{Areal}_{\mathrm{expansion}}(E) = \left(\frac{\mathrm{area}_{\mathrm{E}}}{\mathrm{area}_{\mathrm{OCV}}} - 1\right) \times 100 \quad (1)$$

where the areal expansion is a function of the voltage E, and $\mathrm{area}_{\mathrm{E}}$ is the area of the tin particle at voltage E, and $\mathrm{area}_{\mathrm{ocv}}$ is the area of the pristine particle at the open circuit voltage (before lithiation).

The areal expansion of this dense tin grain was quantified from these images, using ImageJ, and is plotted as a function of voltage (Figure 4c, black squares). The areal expansion of this particle increases by 9% at 0.28 V followed by a large expansion to 134% of its original size by 0.05 V. Assuming spherical symmetry and homogeneous expansion, geometrically the volume expansion can be estimated from the areal expansion through the geometric relationship in eq 2

$$\%\mathrm{Volume}_{\mathrm{expansion}} = \left(\sqrt[\frac{3}{2}]{\frac{\mathrm{area}_{\mathrm{E}}}{\mathrm{area}_{\mathrm{OCV}}}} - 1\right) \times 100 \quad (2)$$

Using eq 2, the calculated volume expansion is 260% of its original size, which is in agreement with previous reports on tin-based materials.[42] Another consideration that affects the reversibility in dense tin is that the volume change mostly occurs at the end of the insertion process, which is also consistent with previous reports.[31] This accelerated expansion is one factor responsible for crack formation, seen in our TXM images, which expose new surfaces to the electrolyte that can undergo reaction with the electrolyte.[31] Figure 4c shows that the particle does not contract back to its original size, most likely because there are nonaccessible Li-rich domains within the particle that are either electrically insulated or physically separated from the slurry matrix.[38]

The dramatic expansion observed for dense tin is significantly reduced in NP-Sn (Figure 4a, bottom). The areal expansion of this ~5 μm NP-Sn grain was quantified from these images and plotted as a function of voltage (Figure 4c, green circles). The areal expansion, defined similarly as above, is only 21% compared to the 134% expansion for dense tin, a 6-fold decrease. We have estimated this areal expansion to correspond to a volume expansion increase of only 33% of the original size using eq 2. While this geometric relationship is strictly only valid for spherical symmetry, this analysis does at least provide a reasonable estimation of the volume expansion. As a result of the decreased expansion, no cracks formed during the lithiation or delithiation process. We have also plotted the areal expansion of another larger particle (Figure 4c, red triangles) with a diameter of ~10 μm (particle is shown in Figure 5) at the lithiated and delithiated state only. This larger particle appears to expand somewhat more than the smaller particle (50% areal expansion and 84% volume expansion in the lithiated state) but still contracts back nearly to its original size in the delithiated state (remains just 17% expanded). A full expansion set was not collected on this particle because the edges were in poor focus, making it hard to determine the area. While the expansion apparently depends somewhat on the size of the NP-Sn particles, the areal expansion in this larger tin particle is still nearly 3-fold less than the dense tin and much more reversible. The dominating mechanism for both the reduced expansion and the increase reversibility in these porous particles probably derives from the open porous network that is both flexible, and accommodates the expanding ligaments.

DOI: 10.1021/acs.nanolett.6b04181
Nano Lett. 2017, 17, 870−877

As we mentioned previously, the internal porosity of NP-Sn is ~25%. As a result of this porosity, electrolyte penetrates into the particle and deinsertion is also much more reversible in NP-Sn compared to dense tin. NP-Sn recovers 728 mAh/g capacity while dense tin only recovers 588 mAh/g. This disparity in utilization can be directly seen in the series of TXM images corresponding to the deinsertion process (Figure 4b, top). In contrast to dense tin, which only contracts slightly, the NP-Sn grain contracts back nearly to the same total area as the pristine NP-Sn grain (Figure 4b, bottom). These direct structural observations lead to the understanding that the nanoscale porosity and mechanical flexibility are responsible for the overall reduced expansion and better reversibility, which in turn leads to better utilization of the active material. The long lifetime observed for NP-Sn is most likely strongly influenced by both factors observed here.

Another structural feature of the NP-Sn particle shown in Figure 4b and quantified in Figure 4c is that it begins to expand sooner (at higher voltage) compared to dense tin, which indicates that the nanoscale architecture influences the lithiation kinetics. The time-scale of the lithiation process in a diffusion controlled system, such as the lithiation of tin, is proportional to the diffusion length squared.[57] Therefore, decreasing the diffusion length by one order of magnitude (e.g., 1 μm to 100 nm) should have an amplified effect of reducing the lithiation time-scales in the nanoporous material by two orders of magnitude. As a result, the faster kinetics in NP-Sn most likely leads to a more homogeneous lithiation process compared to dense tin, which may lead to the enhanced cycle lifetimes.

In order to further understand the role of porosity in enabling long-term cycle life, a population of individual pores were monitored in a single NP-Sn grain during cycling. While pores are observed in the particle shown in Figure 4, those pores are hard to discern and quantify due to the small particle size. To monitor changes in the pores better, we chose to analyze the larger 10 μm NP-Sn grain also shown in Figure 4. The center of this NP-Sn grain was in excellent focus throughout cycling and underwent an expansion similar to the smaller ~5 μm NP-Sn particle (Figure 5a).

The evolution of pore size and pore size distribution in a NP-Sn grain during cycling is shown in Figure 5. Because the same particle is imaged during lithium insertion and deinsertion, the same pores within the NP-Sn particle can be tracked during cycling. As mentioned earlier, the 2D images used in these analyses are projections of the NP-Sn 3D morphology, so we again represent the change in pore sizes in terms of pore area. Because the 2D TXM images are projections of a 3D morphology, the exact pore size and shape cannot be determined exactly from these images. However, they do give a representative size and can be used to clearly discern changes to the pore system during lithiation and delithiation. We point out that the pores in these absorption based images are distinguished as the dark spots while the lighter portions are the solid ligaments. The clear contrast between the pores and the solid regions enables the pore system to be statistically quantified using image analysis software.

The images shown in Figures 5a–d and S3 were used to calculate the statistical information presented in Figure 5e,f. Figure 5a shows an image of our pristine 10 μm grain. Figure 5b–d shows expanded images of a smaller region of the same grain in the pristine, lithiated, and delithiated states. The expanded images were used for statistical analysis. To analyze the images, a series of histograms (number of pores versus individual pore area) were calculated and are shown in Figure S4. These histograms were then used to calculate the average pore area and the standard deviation of pore area at each voltage plateau, as shown in Figure 5e,f. The average pore area shows the evolution of the average pore size with lithium insertion and deinsertion. The NP-Sn grain before cycling contains mostly pores that are <50 nm, as seen in the histogram of pristine (OCV) NP-Sn in Figure S4. As lithiation proceeds, the number of small pores decreases as some pores grow into the 100–200 nm size range. This produces an increase in average pore size, and a broader pore size distribution. In agreement with the histograms presented in Figure S4, both the average pore size (Figure 5 e) and pore size distribution (Figure 5 f), increases during the first charge and discharge, though the change is not fully monotonic.

To more fully understand the changes in porosity, the pores in the NP-Sn grain in the lithiated state can be sorted into two groups: a population of pores that are similar in size to the original porosity before cycling, and a population of larger pores that form as a result of the expansion process. This observation of an increase in pores size is in good agreement with previous work,[58] but it is interesting to find that only part of the pores increase in size upon lithiation. During delithiation, both the average pore size and the distribution remain relatively unchanged up to 0.58 V and then drop significantly at 0.65 V as significant amounts of lithium start to leave the structure. Presumably, the drop in pore size and size distribution at 0.65 V is due to the contraction of NP-Sn grain as higher density tin phases replace lithiated tin. As even more lithium is removed, the bimodal pore size distribution becomes more prominent and both the average pores size and the standard deviation again increase due to a population of very large pores. We hypothesize that the large pores are caused by pore fusion and cracking due to the strain association with pore expansion and contraction. Less strained pores survive the expansion on contraction without fusion, resulting in the overserved bimodal pore size distribution as seen in the 1 V histogram (Figure S4). Potentially, the mechanical flexibility afforded by the smaller pores prevents even more pore evolution, like what is observed in bulk systems. Indeed, like the smaller particle shown in Figure 4, no cracks were observed throughout the cycle (Figure S3). These results thus suggest that pore size, pores size distribution, and total grain size all need to be optimized to produce the most stable cycling.

A final feature of the images shown in Figure 5 is that the pores appear to remain interconnected throughout the Li alloying and dealloying process. Having an interconnected pore and ligament architecture during charge and discharge is required for good performance. While 3D reconstructions, rather than the 2D images shown here, would provide more conclusive evidence of connectivity, we found that the samples could not handle the X-ray dose required for tomographic imaging. The 2D TXM images of the NP-Sn, however, do clearly show that the pores do not fully close in the fully lithiated state. Closed pores would prevent effective electrolyte access to the interior of the material, resulting in inhomogeneous Li-ion concentrations, and therefore volume expansion mismatches, which contributes the mechanical failure of bulk materials. In total, several different structural properties all synergistically couple to enable the volume change accommodation and long cycle lifetime in NP-Sn.

DOI: 10.1021/acs.nanolett.6b04181
Nano Lett. 2017, 17, 870–877

Overall, we found that TXM is a powerful method for evaluating the structural evolution that occurs when both dense micrometer size grains of tin and nanoporous tin when alloyed with Li. The majority of the degradation in dense tin occurs in the first insertion process. The degradation is exacerbated by the fact that dense tin undergoes a burst expansion upon lithiation, which is mainly attributed to large diffusion lengths and slow diffusion kinetics inherent to dense materials. This process leads to crack formation and presumably thick SEI growth after multiple expansion and cracking cycles. We speculate that the mechanical stability of the carboxymethyl cellulose binder/carbon fiber matrix is irreversibly deformed during the expansion process and cannot fully contract during the deinsertion process. Ultimately this process may lead to the active material losing electrical contact with the slurry, resulting in a swift capacity decay.[38]

In stark contrast, we observed that NP-Sn undergoes significantly smaller expansion compared to dense tin. The nanoscale ligaments effectively provide short diffusion pathlengths, which enable homogeneous lithiation. There were no manifestations of cracks during the lithiation and delithiation process of NP-Sn. The pore volume accommodates the lower density Li-rich phases effectively enabling a six-fold reduction in the areal expansion. We have also demonstrated that NP-Sn particles remain porous in the fully lithiated state. This is an important finding of this study because a closed pore system is not effective at accommodating volume expansion and does not allow the electrolyte to access the active materials between the pores. The synergy between the small interconnected ligaments and the optimal pore space in NP-Sn, combined with the intrinsic flexibility of porous materials, lessen the aggressive failure mechanisms observed in dense tin.[59,60]

Importantly, the conclusions reported here are likely to be generally applicable to other alloy-type anode materials, even if those materials are too low Z to be directly imaged using TXM. We envision that other materials like silicon, antimony, and germanium would benefit from the nanoscale architecture found to be optimal in tin-based electrodes. Importantly, our results show that simply adding porosity alone is not sufficient. There appears to be a complex interplay between the pore size, the pore size distribution, and the total particle size with 5 μm particles showing better reversibility than 10 μm grains. While this complexity may seem daunting, it highlights the potential to use direct imaging to guide the creation of porous anode materials with truly optimized architectures and cycling behavior using highly scalable methods like the dealloying employed here.

■ ASSOCIATED CONTENT

Supporting Information

The Supporting Information is available free of charge on the ACS Publications website at DOI: 10.1021/acs.nanolett.6b04181.

Materials and methods, XRD data on nanoporous Sn, and additional SEM characterization of the electrodes used for TXM imaging (PDF)

■ AUTHOR INFORMATION

Corresponding Author

*E-mail: tolbert@chem.ucla.edu.

ORCID

Sarah H. Tolbert: 0000-0001-9969-1582

Present Address

⊥Department of Materials Science and Engineering, University of Pennsylvania, 3231 Walnut St., Philadelphia, PA 19104-6272, USA

Author Contributions

J.B.C. and T.C.L. contributed to the work equally. J.B.C. and S.H.T conceived and planned the experiment. J.B.C., T.C.L., and J.N.W. carried out the transmission X-ray microscopy measurements. J.B.C., T.C.L., J.N.W., and S.H.T. performed the image analysis and interpretation. E.D. developed and prepared the nanoporous tin. All authors prepared the manuscript.

Author Contributions

J.B.C. and T.C.L. contributed to this work equally.

Notes

The authors declare no competing financial interest.

■ ACKNOWLEDGMENTS

This work was supported by the U.S. Department of Energy, Office of Science, Basic Energy Sciences, under Award Number DE-SC0014213. Use of the Stanford Synchrotron Radiation Lightsource, SLAC National Accelerator Laboratory, is supported by the U.S. Department of Energy, Office of Science, Office of Basic Energy Sciences, under Contract No. DE-AC02-76SF00515. Engineering support from Dr. D. Van Campen at end-station 6-2C at SSRL is gratefully acknowledged.

■ REFERENCES

(1) Sivakkumar, S. R.; Milev, A. S.; Pandolfo, A. G. *Electrochim. Acta* **2011**, *56*, 9700−9706.
(2) Endo, M.; Kim, C.; Nishimura, K.; Fujino, T.; Miyashita, K. *Carbon* **2000**, *38*, 183−197.
(3) Scrosati, B. *J. Electrochem. Soc.* **1992**, *139*, 2776−2781.
(4) Ozawa, K. *Solid State Ionics* **1994**, *69*, 212−221.
(5) Nitta, N.; Yushin, G. *Part. Part. Syst. Charact.* **2014**, *31*, 317−336.
(6) Sivakkumar, S. R.; Nerkar, J. Y.; Pandolfo, A. G. *Electrochim. Acta* **2010**, *55*, 3330−3335.
(7) Buqa, H.; Goers, D.; Holzapfel, M.; Spahr, M. E.; Novák, P. *J. Electrochem. Soc.* **2005**, *152*, A474−A481.
(8) Jia, H.; Gao, P.; Yang, J.; Wang, J.; Nuli, Y.; Yang, Z. *Adv. Energy Mater.* **2011**, *1*, 1036−1039.
(9) McDowell, M. T.; Lee, S. W.; Nix, W. D.; Cui, Y. *Adv. Mater.* **2013**, *25*, 4966−4985.
(10) Chan, C. K.; Peng, H.; Liu, G.; McIlwrath, K.; Zhang, X. F.; Huggins, R. A.; Cui, Y. *Nat. Nanotechnol.* **2008**, *3*, 31−35.
(11) Larcher, D.; Beattie, S.; Morcrette, M.; Edström, K.; Jumas, J.-C.; Tarascon, J.-M. *J. Mater. Chem.* **2007**, *17*, 3759−3772.
(12) Zhang, W. J. *J. Power Sources* **2011**, *196*, 13−24.
(13) Park, C.-M.; Kim, J.-H.; Kim, H.; Sohn, H.-J. *Chem. Soc. Rev.* **2010**, *39*, 3115−3141.
(14) Wen, C. J.; Hugglns, R. A. *J. Electrochem. Soc.* **1981**, *128*, 1181−1187.
(15) Courtney, I. A.; Dahn, J. R. *J. Electrochem. Soc.* **1997**, *144*, 2045−2052.
(16) Huggins, R. A.; Nix, W. D. *Ionics* **2000**, *6*, 57−63.
(17) Beaulieu, L. Y.; Eberman, K. W.; Turner, R. L.; Krause, L. J.; Dahn, J. R. *Electrochem. Solid-State Lett.* **2001**, *4*, A137−A140.
(18) Besenhard, J. O.; Yang, J.; Winter, M. *J. Power Sources* **1997**, *68*, 87−90.
(19) Huang, J. Y.; Zhong, L.; Wang, C. M.; Sullivan, J. P.; Xu, W.; Zhang, L. Q.; Mao, S. X.; Hudak, N. S.; Liu, X. H.; Subramanian, A.; Fan, H.; Qi, L.; Kushima, A.; Li, J. *Science* **2010**, *330*, 1515−1521.

DOI: 10.1021/acs.nanolett.6b04181
Nano Lett. 2017, 17, 870−877

(20) Liu, X. H.; Zheng, H.; Zhong, L.; Huang, S.; Karki, K.; Zhang, L. Q.; Liu, Y.; Kushima, A.; Liang, W. T.; Wang, J. W.; Cho, J.-H.; Epstein, E.; Dayeh, S. A.; Picraux, S. T.; Zhu, T.; Li, J.; Sullivan, J. P.; Cumings, J.; Wang, C.; Mao, S. X.; Ye, Z. Z.; Zhang, S.; Huang, J. Y. *Nano Lett.* **2011**, *11*, 3312−3318.
(21) Sethuraman, V. A.; Chon, M. J.; Shimshak, M.; Srinivasan, V.; Guduru, P. R. *J. Power Sources* **2010**, *195*, 5062−5066.
(22) Ding, L.; He, S.; Miao, S.; Jorgensen, M. R.; Leubner, S.; Yan, C.; Hickey, S. G.; Eychmüller, A.; Xu, J.; Schmidt, O. G. *Sci. Rep.* **2014**, *4*, 1−8.
(23) Im, H. S.; Cho, Y. J.; Lim, Y. R.; Jung, C. S.; Jang, D. M.; Park, J.; Shojaei, F.; Kang, H. S. *ACS Nano* **2013**, *7*, 11103−11111.
(24) Xu, L.; Kim, C.; Shukla, A. K.; Dong, A.; Mattox, T. M.; Milliron, D. J.; Cabana, J. *Nano Lett.* **2013**, *13*, 1800−1805.
(25) Cook, J. B.; Detsi, E.; Liu, Y.; Liang, Y.-L.; Kim, H.; Petrissans, X.; Dunn, B. S.; Tolbert, S. H. *ACS Appl. Mater. Interfaces* **2016**, DOI: 10.1021/acsami.6b09014.
(26) Detsi, E.; Tolbert, S. H.; Punzhin, S.; De Hosson, J. T. M. *J. Mater. Sci.* **2016**, *51*, 615−634.
(27) Nishio, K.; Tagawa, S.; Fukushima, T.; Masuda, H. *Electrochem. Solid-State Lett.* **2012**, *15*, A41−A44.
(28) Ge, M.; Fang, X.; Rong, J.; Zhou, C. *Nanotechnology* **2013**, *24*, 422001.
(29) Kim, H.; Han, B.; Choo, J.; Cho, J. *Angew. Chem., Int. Ed.* **2008**, *47*, 10151−10154.
(30) Yu, Y.; Gu, L.; Zhu, C.; Tsukimoto, S.; van Aken, P. A.; Maier, J. *Adv. Mater.* **2010**, *22*, 2247−2250.
(31) Jia, H.; Gao, P.; Yang, J.; Wang, J.; Nuli, Y.; Yang, Z. *Adv. Energy Mater.* **2011**, *1*, 1036−1039.
(32) Chen, W.; Fan, Z.; Dhanabalan, A.; Chen, C.; Wang, C. *J. Electrochem. Soc.* **2011**, *158*, A1055−A1059.
(33) Liu, N.; Huo, K.; McDowell, M. T.; Zhao, J.; Cui, Y. *Sci. Rep.* **2013**, *3*, 1−7.
(34) Ba, J.; Polleux, J.; Antonietti, M.; Niederberger, M. *Adv. Mater.* **2005**, *17*, 2509−2512.
(35) Jiao, Y.; Han, D.; Ding, Y.; Zhang, X.; Guo, G.; Hu, J.; Yang, D.; Dong, A. *Nat. Commun.* **2015**, *6*, 6420.
(36) Etacheri, V.; Seisenbaeva, G. A.; Caruthers, J.; Daniel, G.; Nedelec, J.-M.; Kessler, V. G.; Pol, V. G. *Adv. Energy Mater.* **2015**, *5*, 1401289.
(37) Shearing, P. R.; Howard, L. E.; Jørgensen, P. S.; Brandon, N. P.; Harris, S. J. *Electrochem. Commun.* **2010**, *12*, 374−377.
(38) Weker, J. N.; Liu, N.; Misra, S.; Andrews, J. C.; Cui, Y.; Toney, M. F. *Energy Environ. Sci.* **2014**, *7*, 2771−2777.
(39) Nelson Weker, J.; Toney, M. F. *Adv. Funct. Mater.* **2015**, *25*, 1622−1637.
(40) Nelson, J.; Misra, S.; Yang, Y.; Jackson, A.; Liu, Y.; Wang, H.; Dai, H.; Andrews, J. C.; Cui, Y.; Toney, M. F.; Andrews, J. C. *J. Am. Chem. Soc.* **2012**, *134*, 6337−6343.
(41) Wang, J.; Chen-Wiegart, Y.-C. K.; Wang, J. *Angew. Chem., Int. Ed.* **2014**, *53*, 4460−4464.
(42) Ebner, M.; Marone, F.; Stampanoni, M.; Wood, V. *Science* **2013**, *342*, 716−720.
(43) Chao, S. C.; Song, Y. F.; Wang, C. C.; Sheu, H. S.; Wu, H. C.; Wu, N. L. *J. Phys. Chem. C* **2011**, *115*, 22040−22047.
(44) Chao, S. C.; Yen, Y. C.; Song, Y. F.; Chen, Y. M.; Wu, H. C.; Wu, N. L. *Electrochem. Commun.* **2010**, *12*, 234−237.
(45) Ruther, R. E.; Dixit, H.; Pezeshki, A. M.; Sacci, R. L.; Cooper, V. R.; Nanda, J.; Veith, G. M. *J. Phys. Chem. C* **2015**, *119*, 18022−18029.
(46) Cook, J. B.; Kim, H.-S.; Yan, Y.; Ko, J. S.; Robbennolt, S.; Dunn, B.; Tolbert, S. H. *Adv. Energy Mater.* **2016**, *6*, 1501937.
(47) Kim, H.-S.; Cook, J. B.; Tolbert, S. H.; Dunn, B. *J. Electrochem. Soc.* **2015**, *162*, A5083−A5090.
(48) Becker, C. R.; Strawhecker, K. E.; McAllister, Q. P.; Lundgren, C. A. *ACS Nano* **2013**, *7*, 9173−9182.
(49) Luo, Y.; Cai, W.-B.; Scherson, D. a. *Electrochem. Solid-State Lett.* **2001**, *4*, A101−A104.
(50) Barrett, E. P.; Joyner, L. G.; Halenda, P. P. *J. Am. Chem. Soc.* **1951**, *73*, 373−380.
(51) Brunauer, S.; Deming, L. S.; Deming, W. E.; Teller, E. *J. Am. Chem. Soc.* **1940**, *62*, 1723−1232.
(52) Jia, H.; Gao, P.; Yang, J.; Wang, J.; Nuli, Y.; Yang, Z. *Adv. Energy Mater.* **2011**, *1*, 1036−1039.
(53) Rhodes, K. J.; Meisner, R.; Kirkham, M.; Dudney, N.; Daniel, C. *J. Electrochem. Soc.* **2012**, *159*, A294−A299.
(54) Winter, M.; Besenhard, J. O. *Electrochim. Acta* **1999**, *45*, 31−50.
(55) Wang, J.; Huggins, R. A. *J. Electrochem. Soc.* **1986**, *133*, 457−460.
(56) Endo, M.; Kim, Y. A.; Hayashi, T.; Nishimura, K.; Matusita, T.; Miyashita, K. *Carbon* **2001**, *39*, 1287−1297.
(57) Zhang, H.; Yu, X.; Braun, P. V. *Nat. Nanotechnol.* **2011**, *6*, 277−281.
(58) Chen, Q.; Sieradzki, K. *Nat. Mater.* **2013**, *12*, 1102−1106.
(59) Detsi, E.; Punzhin, S.; Rao, J.; Onck, P. R.; De Hosson, J. T. M. *ACS Nano* **2012**, *6*, 3734−3744.
(60) Biener, J.; Hodge, A.; Hayes, J. *Nano Lett.* **2006**, *6*, 2379−2382.

DOI: 10.1021/acs.nanolett.6b04181
Nano Lett. 2017, 17, 870−877